Dual-beam laser thermal processing of silicon photovoltaic materials

Brian J. Simonds*[a], Anthony Teal[b], Tian Zhang[b], Josh Hadler[a], Zibo Zhou[b], Sergey Varlamov[b], Ivan Perez-Würfl[b]

[a]National Institute of Standards and Technology, 325 Broadway, Boulder, CO 80305-3337; [b]School of Photovoltaic and Renewable Energy Engineering, Faculty of Engineering, The University of New South Wales, Sydney, Australia 2052

ABSTRACT

We have developed an all-laser processing technique by means of two industrially-relevant continuous-wave fiber lasers operating at 1070 nm. This approach is capable of both substrate heating with a large defocused beam and material processing with a second scanned beam, and is suitable for a variety of photovoltaic applications. We have demonstrated this technique for rapid crystallization of thin film (~10 μm) silicon on glass, which is a low cost alternative to wafer-based solar cells. We have also applied this technique to wafer silicon to control dopant diffusion at the surface region where the focused line beam rapidly melts the substrate that then regrows epitaxially. Finite element simulations have been used to model the melt depth as a function of preheat temperature and line beam power. This process is carried out in tens of seconds for an area approximately 10 cm^2 using only about 1 kW of total optical power and is readily scalable. In this paper, we will discuss our results with both c-Si wafers and thin-film silicon.

Keywords: crystallization, dopant diffusion, Laser processing, photovoltaics, silicon

1. INTRODUCTION

A recent analysis of the photovoltaic (PV) industry found that advancements in manufacturing technology are key to long-term competitiveness for PV manufacturers[1]. Meanwhile, industrial scale laser processing has become more prevalent in many manufacturing sectors due to its versatility, precision, and speed. These attributes lead to lower manufacturing costs, increased product yield and higher product throughput. Realizing these benefits in the extremely competitive PV industry would clearly lead to a competitive advantage, as well as achieve many of the goals set forth by the US Department of Energy SunShot program[2].

Laser processing for solar cells has been traditionally used for very small dimensional features where focused beams are rastered to create lines for edge isolation, scribing, and selective emitter formation and for drilling holes in wrap-through style cells. Larger area laser applications, for instance in liquid-phase crystallization of thin film Si on glass (LPCSG), are currently under investigation; however, these rely on additional isothermal heat input. In this work, we describe a newly developed dual-beam laser technique that is capable of treating large area PV materials. This technique is appropriate in situations that require large area heating in conjunction with focused laser processing. To demonstrate this approach, we applied it to LPCSG as well as dopant diffusion in crystalline silicon (cSi). The former is an approach where a focused laser is used to melt a layer of amorphous silicon (aSi) about 10 μm thick, which then crystallizes upon solidification. Current approaches require a preheat by means of a hot-plate to improve film adhesion[3], which ultimately limits its large scale utility. Our technique could overcome this limitation. The second application to cSi wafers would supplant a very time consuming PV manufacturing step where a long (tens of minutes) furnace anneal is used to diffuse dopants. Reducing the time of this step would increase PV module throughput and therefore decrease manufacturing cost per Watt.

Laser Applications in Microelectronic and Optoelectronic Manufacturing (LAMOM) XXI, edited by Beat Neuenschwander, Stephan Roth, Costas P. Grigoropoulos, Tetsuya Makimura, Proc. of SPIE Vol. 9735, 973505 · © 2016 SPIE · CCC code: 0277-786X/16/$18 · doi: 10.1117/12.2213583

2. EXPERIMENT

2.1 Dual beam laser processing

The lasers used for these experiments were continuous-wave ytterbium fiber lasers that operated at 1070 nm, or 1.16 eV. A diagram of the experimental configuration is shown in Figure 1a with a picture shown in Figure 1b. Beam #1 was sent through two cylindrical lenses (l1 and l2, focal length = -75.6 mm) that were rotated 90 degrees with respect to one another in order to expand and elongate the beam along the scan direction. This beam served to preheat the sample. The temperature of the sample was continuously monitored by an infrared pyrometer with emissivity set to 0.8, and was focused on the center of the sample. This reading was used to manually adjust the optical power in beam #1 until the desired preheat temperature was achieved. Experimentally, we used preheat temperatures between 100 °C and 725 °C, which corresponded to applied optical powers for beam #1 between 150 W and 750 W. A typical temperature profile for cSi is shown in Figure 2, where one can see very rapid heating with a temperature gradient over 110 °C/s. The sharp increase in temperature seen around 50 s is due to the focused laser beam incident on the opposite side as the pyrometer. Due to the relatively slow response time of the pyrometer (1 s) and the rapid scan of the focused beam, this peak is not representative of the actual peak temperature achieved during processing. A much more gradual heating and cooling ramp was used for the LPCSG samples due to the mismatch of thermal expansion coefficients of the glass substrate and aSi in order to help prevent cracking.

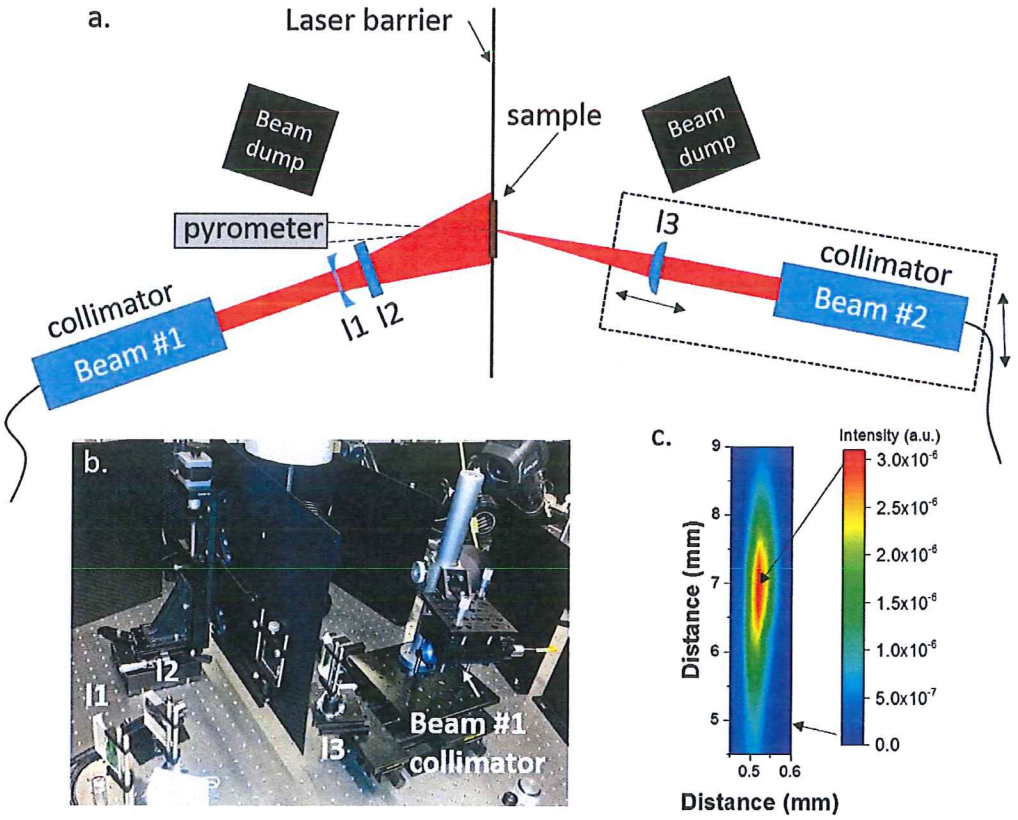

Figure 1: A diagram of the experimental setup is shown in part a. The preheat laser (beam #1) was delivered by optical fiber to a collimator followed by two 90° opposed cylindrical lenses. The focused process beam (beam #2) was made into a line beam with a single cylindrical lens. An infrared pyrometer was used to constantly monitor the temperature of the sample. A photograph of the arrangement is shown in b. A pinhole scan of the focused line beam with a photodiode was used to create the focused beam profile at the sample plane shown in c, which reveals a stretched Gaussian beam.

Materials processing was achieved by beam #2, which following collimation, was focused to a sharp vertical line at the sample using a cylindrical lens (l3) with a focal length of 75 mm. The collimator and focusing optic were placed on a single fixture mounted to a translational stage (dashed box, vertical motion in Figure 1a.). This allowed for the scanning of beam #2 across the sample in such a way that the sample always saw the same beam profile. Both laser beams were slightly off normal incidence by 17° to ensure that back reflections from the sample were not coupled back into the lasers. The sample was placed in an aluminum holder mounted to a hole in a laser barrier that prevented the two beams from being coupled to one another. The profile of the laser beam was measured by placing a photodiode with a 25 μm pinhole aperture at the sample position, and rastering it through an attenuated line beam. The resulting contour map of the beam #1 intensity is shown in Figure 1c. This reveals a stretched Gaussian beam with full width at half maximum at the peak intensity of 53.3 μm and 2.25 mm, for both horizontal and vertical directions, respectively. By repeating this measurement at different planes along the propagation direction, the depth of focus was found to be about 1 mm.

The two material systems used to test the dual laser beam approach are thin film aSi on glass and a cSi wafer. The aSi samples were prepared by electron-beam evaporation of 10 μm of silicon at 650 °C on top of 3.3 mm borosilicate glass containing a $SiO_x/SiN_x/SiO_x$ buffer layer. More detailed sample preparation instructions for the aSi films can be found elsewhere[4,5]. The p-type wafers were 500 μm thick and polished on both sides. Their background doping concentration was $1x10^{16}$ cm^{-3} with furnace diffused phosphorous 400 nm deep and an $8x10^{19}$ cm^{-3} surface concentration. Photoluminescence (PL) imaging was performed on the laser-crystallized aSi in a similar manner as described elsewhere[6].

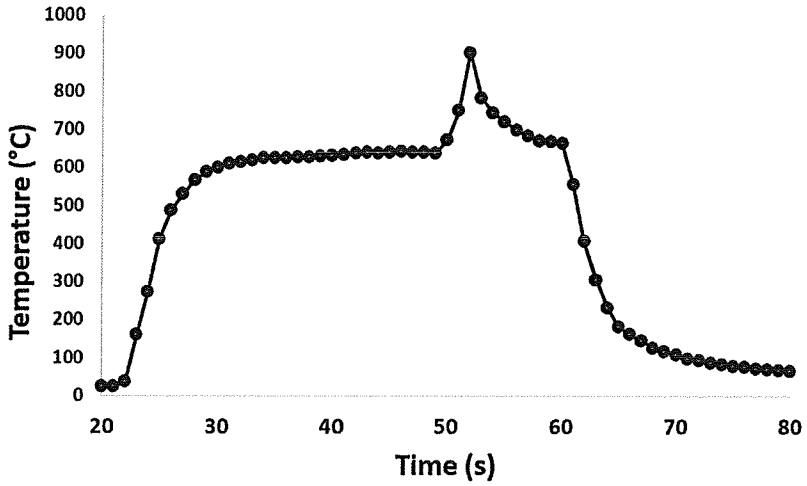

Figure 2: A typical plot of the temperature versus time for the dual laser beam treatment of cSi that shows the rapid heating and cooling that can be achieved with this technique.

2.2 Finite Element Simulations

A finite element simulation tool was developed using COMSOL Multiphysics[7] to determine the melt depths in cSi as a function of different laser parameters. The general idea of such a model is to couple the heat-transfer equation to heat input due to optical absorption. The partial differential equations and parameters used in the simulations are given in Table 1. Material properties like heat capacity (C_p), density (ρ), thermal conductivity (k), and reflectivity (R) are given as functions of temperature both above and below the silicon melting point (T_{melt}) and were ascribed to a 1 cm x 1 cm x 500 μm thick rectangular parallelepiped. A phase transition at T_{melt} is accomplished by including the latent heat of melting, L_m, in C_p. The absorption coefficient, α, is treated as constant although this is not strictly true. However, since there is insufficient experimental or theoretical data for α near the melting point, we have opted to use a value of 1000 cm^{-1}, which is predicted for cSi around 700 °C for 1070 nm light based on thermal expansion and the subsequent bandgap narrowing[8]. The spatial parameters for the laser beam were taken from Gaussian fits to the pinhole scans shown in Figure 1c., which acted as a moving heat input, Q, with velocity v_x. The effect of the preheat beam was applied by specifying the temperature at the

rear boundary as opposed to modeling a specific optical absorption. This temperature along with line beam power, P_0, and v_x were systematically varied to investigate their effects on the melt depth in the cSi wafer. In principle, a similar model could be used to investigate the qualitative behavior of the melting of aSi on glass. However, since the temperature-dependent thermal and optical properties of aSi are less well known than for cSi, the results would be much less reliable.

Table 1: Parameters and equations used for finite element simulations

Parameter	Equation	Source
Heat Transport Equation	$\rho(T)C_p(T)\frac{\partial T}{\partial t} + \rho(T)C_p(T)\boldsymbol{u}\cdot\nabla T - \nabla k(T)T = Q$	[9]
Heat input, Q	$\frac{P_0}{2\pi * \sigma_x\sigma_y}(1 - R(T))\alpha e^{-\alpha z}e^{-(x-v_x t)^2/2\sigma_x{}^2}e^{-y^2/2\sigma_y{}^2}$	[9]
$Cp(T) < T_{melt}$	(.158 + 3.13x10^{3}*T - 5.60x10^{-6}*T^2 + 5.22x10^{-9}*T^3 - 2.40x10^{-12}*T^4 + 4.29x10^{-16}*T^5) J/(g*K)	[10]
$Cp(T) > T_{melt}$	.9685 J/(g*K)	[10]
$\rho(T) < T_{melt}$	(2330 + .484*T + 1.98*T^2) kg/m^3	[11]
$\rho(T) > T_{melt}$	(2885 - .1925*T) kg/m^3	[11–20]
$k(T) < T_{melt}$	(95.44 – 0.0969*T + 3.27x10^{5}*T^2) W/(m*K)	[21–23]
$k(T) > T_{melt}$	50 W/(m*K)	[23]
$R(T) < T_{melt}$	.32	[24]
$R(T) > T_{melt}$	.65	[24]
T_{melt}	1688 K	[25]
σ_x	.0226 mm	data fit
σ_y	.956 mm	data fit
α	1000 cm^{-1}	[8]
Latent heat of melting, L_m	1650 J/g	[10]

3. RESULTS AND DISCUSSION

3.1 Liquid-Phase Crystalline Silicon on Glass

Figure 3 shows results from the LPCSG experiments with a preheat temperature of 160 °C, P_0 = (49.0 ± 1.0) W, and v_x = 2.89 mm/s. Although we tested a wide range of parameters, these resulted in polycrystalline material that gave the brightest PL intensity and were thus believed to be of the best quality made. A full analysis of the complete effects on material quality of different laser annealing parameters will be the topic of future research. The optical images (a. - c.) show the progression from the beginning of the line beam scan (a.) to the end (c.). These images reveal topological features that are dense in the starting zone (a.) with decreasing occurrence towards the end of the scan (c.), which is consistent with previous results[6]. Evidence of polycrystalline material is given by the PL image in Figure 3d. The increased intensity of the laser scanned area shows that we have made polycrystalline material of similar quality to other LPCSG processes as it is noted that solid-phase crystallized polycrystalline Si does not show PL[6].

The substrate temperature during the LPCSG is known to be a key parameter for thin-film quality and adhesion[3,4]. The success of a relatively low temperature used here (160 °C) is surprising compared to the almost 600 °C required for similar materials with a traditional hot plate preheat[3]. Since it is likely that the thermal gradients differ substantially between hot plate and laser preheat treatment, this result could be due to thermally induced mechanical properties. However, a more conclusive statement will require more investigation. In general though, a lower substrate temperature is advantageous as it allows for the use of lower thermal budget substrates.

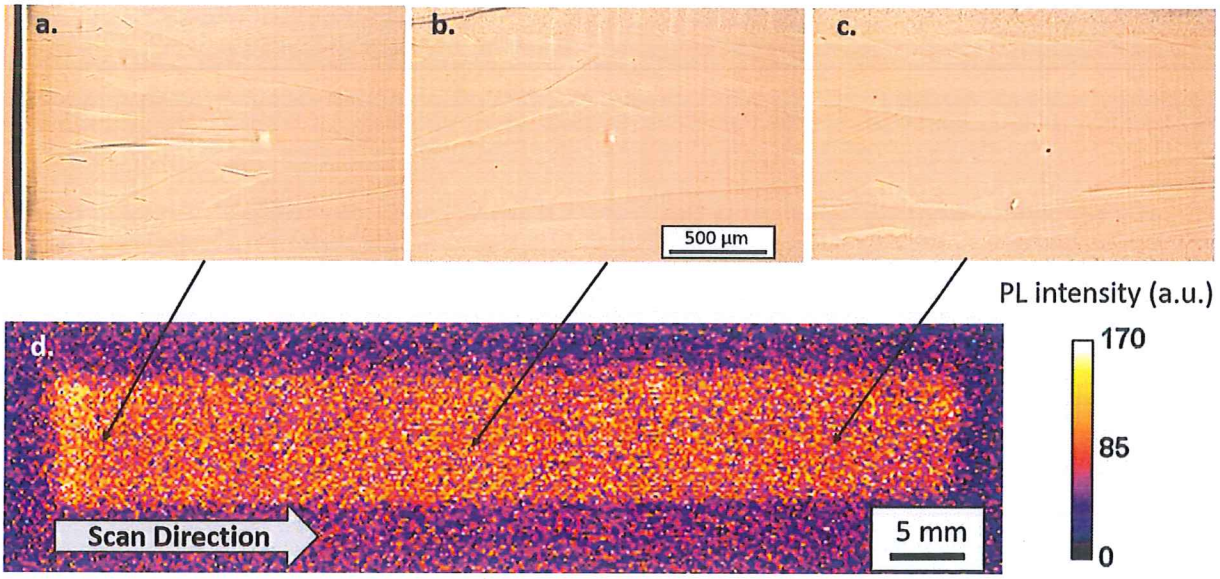

Figure 3: Optical images taken at the beginning (a.), middle (b.) and end (c.) of the laser crystallized film are shown. Photoluminescence imaging of the laser treated area is shown in part d. The bright intensity of the laser crystallized region is in clear contrast to the non-luminescing surrounding amorphous material.

3.2 Rapid Dopant Diffusion in Crystalline Silicon

The dual laser beam process was also applied to a cSi wafer to encourage rapid diffusion of near-surface dopants. Here we take advantage of the fact that impurities diffuse several orders of magnitude faster in molten silicon than in solid[26]. Therefore, we aim to melt a near surface region containing shallow, pre-diffused dopants which are then trapped in place as the molten region epitaxially recrystallizes.

Evidence of the molten region is shown in Figure 4a. where a preferential etch technique[27,28] is applied to a cross-section of a laser-treated sample. Here we assume that the extent of the dopant diffusion is the same as the melt depth, which is justified due to the very large diffusivity enhancement at the melting point (5.7×10^{-4} cm^2/s) versus that at the 625 °C preheat temperature shown here (5.6×10^{-16} cm^2/s)[26]. The line beam power used here was (71.8 ± 1.4) W with a scan speed of 4.89 mm/s, which was the fastest speed achievable by our scan stage. The temperature profile shown in Figure 2 is from this sample.

Finite element simulation results are shown in Figure 4 b., c. and d. These show predicted melt depths along the scan direction of the laser as functions of either preheat temperature (b.), line beam power (c.), and scan speed (d.). For Figure 4b., $v_x = 4.89$ mm/s and $P_0 = 80$ W. For Figure 4c., $v_x = 4.89$ mm/s and the substrate temperature was 700 °C. For Figure 4d., $P_0 = 80$ W and substrate temperature was 700 °C. These results show good order-of-magnitude agreement with the evidence shown in 4a. even though the simplicity of the model neglects factors such as evaporation and surface tension driven convection (Marangoni effect). The effects of these factors will be investigated in later versions of the model. Therefore, these results are only meant to be qualitative of how specific parameters affect melt depth and therefore dopant diffusion. These results show that the melt depth can easily be controlled over a wide range by changing either preheat temperature or line beam power. Additionally, Figure 4d. shows that the speed of the process could be increased as a doubling of the scan speed lowers the melt depth by only about 30%, which could easily be compensated for by adjusting either the preheat temperature or the line beam power. The optimization of these parameters will be key as the large temperature gradients and phase transformation induced by the focused laser beam can lead to significant amounts of residual stress in the material.

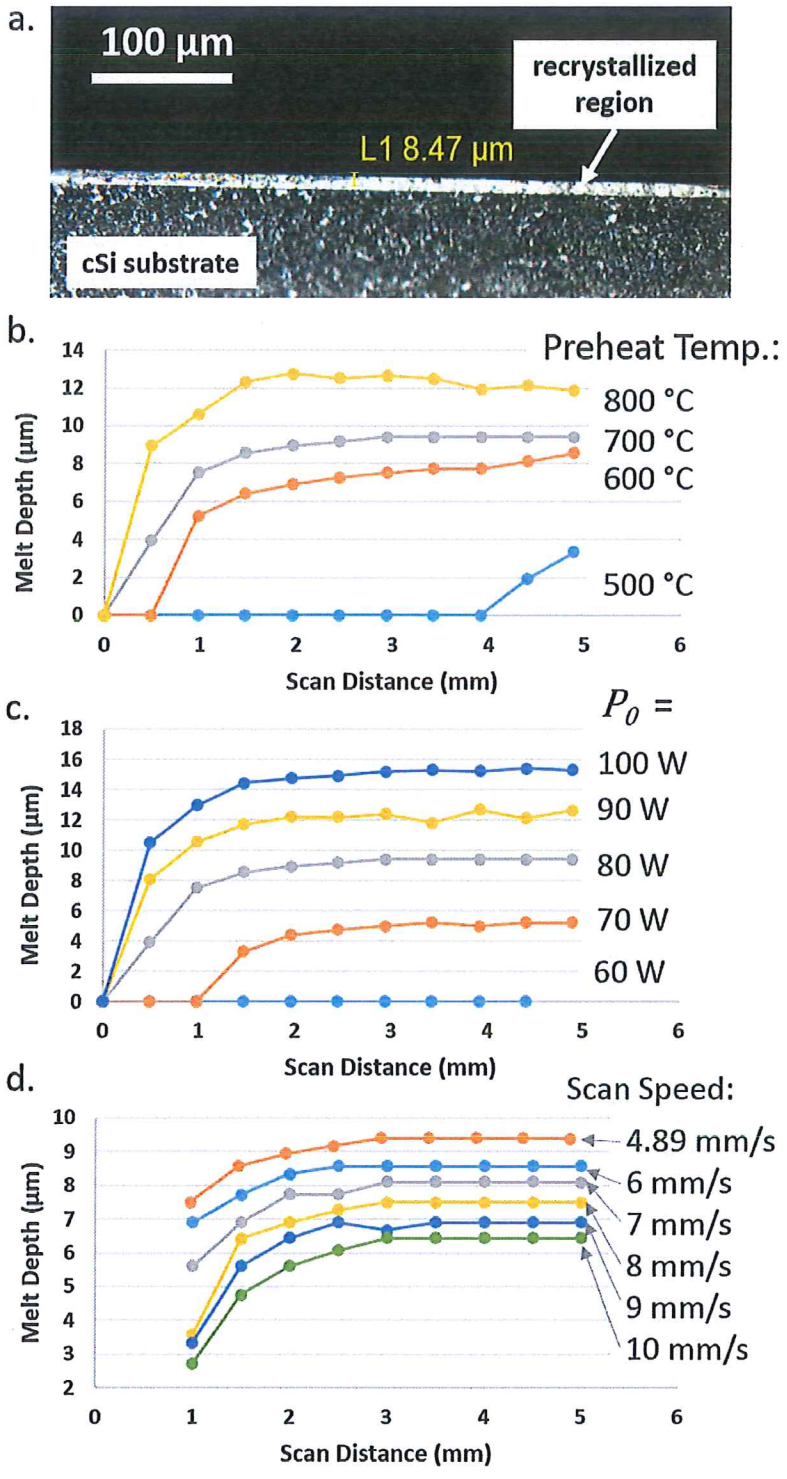

Figure 4: a. Cross-section image following preferential etching to reveal junction, and therefore, melt depth. Finite element simulation results for melt depth along the laser scan direction are shown in parts b., c., and d. as functions of preheat temperature, line beam power, and scan speed, respectively.

4. CONCLUSION

We have presented a novel dual laser beam processing technique and have demonstrated it with two silicon photovoltaic systems. This technique was used to create polysilicon thin film silicon on glass without the need for additional, non-laser heating. From photoluminescence imaging, we showed the presence of polycrystalline material with luminescence similar to that reported in the literature by other approaches. We also demonstrated the ability to melt a shallow surface region in crystalline silicon and rapidly diffuse dopants. To support these experiments, we created a finite element simulation to estimate the melt depth depending on the processing parameters that generally agreed with our experimental results. This simulation was then used to predict the melt depth for a wide range of parameters and demonstrated that the dual laser beam technique is capable of controlling dopant diffusion over a large range of depths.

5. ACKNOWLEDGEMENTS

The authors wish to thank Drs. Kenneth Kroenlein, Boris Wilthan, and Eric Pfeif of the Thermodynamics Research Center at NIST for assistance in choosing the thermophysical properties for use in the simulations.

6. REFERENCES

[1] Goodrich, A. C., Powell, D. M., James, T. L., Woodhouse, M., Buonassisi, T., "Assessing the drivers of regional trends in solar photovoltaic manufacturing," Energy Environ. Sci. **6**, 2811 (2013).

[2] Jones-Albertus, R., Feldman, D., Fu, R., Horowitz, K., Woodhouse, M., "Technology Advances Needed for Photovoltaics to Achieve Widespread Grid Price Parity," Prog. Photovoltaics **in review**.

[3] Varlamov, S., Dore, J., Evans, R., Ong, D., Eggleston, B., Kunz, O., Schubert, U., Young, T., Huang, J., et al., "Polycrystalline silicon on glass thin-film solar cells: A transition from solid-phase to liquid-phase crystallised silicon," Sol. Energy Mater. Sol. Cells **119**, 246–255, Elsevier (2013).

[4] Dore, J., Ong, D., Varlamov, S., Egan, R.., Green, M. A., "Progress in Laser-Crystallised Thin-Film Polycrystalline Silicon Solar Cells," Photovolt. Spec. Conf. (PVSC), 2013 39th IEEE **4**(1), 33–39 (2013).

[5] Dore, J., Ong, D., Varlamov, S., Egan, R., Green, M. A., "Progress in Laser-Crystallized Thin-Film Polycrystalline Silicon Solar Cells: Intermediate Layers, Light Trapping, and Metallization," IEEE J. Photovoltaics **4**(1), 33–39 (2014).

[6] Teal, A., Dore, J., Varlamov, S., "Photoluminescence imaging of thin film silicon on glass," Sol. Energy Mater. Sol. Cells **130**, 1–5, Elsevier (2014).

[7] Software is named for informational purposes only; it does not imply an endorsement or a recommendation by NIST.

[8] Sin, E. H., Ong, C. K., Tan, H. S., "Temperature Dependence of Interband Optical Absorption of Silicon at 1152, 1064, 750 and 694 nm," Phys. Status Solidi **199**, 199–204 (1984).

[9] Yilbas, B. S., Laser Heating Applications: Analytical Modeling (2012).

[10] Desai, P. D., "Thermodynamic Properties of Iron and Silicon," J. Phys. Chem. Ref. Data **15**(3), 967 (1986).

[11] Zhou, Z., Mukherjee, S., Rhim, W. K., "Measurement of thermophysical properties of molten silicon using an upgraded electrostatic levitator," J. Cryst. Growth **257**, 350–358 (2003).

[12] Sasaki, H., Tokizaki, E., Terashima, K., Kimura, S., "Density measurement of molten silicon by an improved Archimedian method," J. Cryst. Growth **139**(3-4), 225–230 (1994).

[13] Sasaki, H., Tokizaki, E., Terashima, K., Kimura, S., "Density Variation of Molten Silicon Measured by an Improved Archimedian Method," Jpn. J. Appl. Phys. **33**(Part 1, No. 7A), 3803–3807 (1994).

[14] Kawanishi, S., Sasaki, H., Terashima, K., Kimura, S., "Effect of Impurity Doping on Density Anomalies in Molten Silicon," Japanese J. Appl. Phys. Part 2 Lett. **34**(Part 2, No. 11B), L1509–L1512 (1995).

[15] Ohsaka, K., Chung, S., "Densities of Si determined by an image digitizing technique in combination with an electrostatic levitator," Appl. Phys. Lett. **70**(4), 423–425 (1997).

[16] Mukai, K., Yuan, Z., "Measurement of the density of molten silicon by a modified sessile drop method," JIM, Mater. Trans. **41**(2), 323–330 (2000).

[17] Sato, Y., Nishizuka, T., Hara, K., Yamamura, T.., Waseda, Y., "Density Measurement of Molten Silicon by a Pycnometric Method," Int. J. Thermophys. **21**(6), 1463–1471 (2000).

[18] Xu, W., Sun, H. C., Xu, J., Li, W., Mu, W. W., Liu, Y., Yan, M. Y., Huang, X. F., Chen, K. J., "Electroluminescence with micro-watt output from ultra-small sized Si quantum dots/amorphous SiO2 multilayers prepared by laser crystallization method," Appl. Surf. Sci. **258**(1), 346–349 (2011).
[19] Watanabe, M., Adachi, M., Morishita, T., Higuchi, K., Kobatake, H.., Fukuyama, H., "Does supercooled liquid Si have a density maximum?," Faraday Discuss. **136**, 279–286; discussion 309–328 (2007).
[20] Vatolin, N. A., Yesin, O. A., "Density of Molten Alloys of Manganese with Silicon, Iron and Carbon," Phys. Met. Metallogr. **16**(6), 129–130 (1963).
[21] Glassbrenner, C. J., Slack, G. A., "Thermal Conductivity of Si and Ge from 3 K to the melting point," Phys. Rev. **134**(4A), A1058–A1069 (1964).
[22] Beers, D. S., Cody, G. D., Abeles, B., "Thermal conductivity of Ge, Si and III-V compounds at high temperatures," Proc. Intern. Conf. Phys. Semicond., 41–48 (1962).
[23] Magomedov, Y. B., Gadjiev, G. G., "High-temperature thermal conductivity of silicon in the solid and liquid states," High Temp. **46**(3), 422–424 (2008).
[24] Hull, R., Properties of Crystalline Silicon, INSPEC, The Institution of Electrical Engineers, London, UK (1999).
[25] Gayler, M. L. V., "Melting Point of High-Purity Silicon," Nature **142**, 478 (1938).
[26] Tang, K., Øvrelid, E. J., Tranell, G., Tangstad, M., "Critical assessment of the impurity diffusivities in solid and liquid silicon," JOM-J. Min. Met. Mat. S. **61**(11), 49–55 (2009).
[27] Jenkins, M. W., "A New Preferential Etch for Defects in Silicon Crystals," J. Electrochem. Soc. **124**(5), 757 (1977).
[28] Fathi, M., "Delineation of Crystalline Extended Defects on Multicrystalline Silicon Wafers," Int. J. Photoenergy **2007**, 1–4 (2007).